





A New Method Exploiting Partial Image Expansion to Include Substrate and Ground in Dipole-Based Near-Field Models

Tomas Monopoli , Xinglong Wu , *Member, IEEE*, Flavia Grassi , *Senior Member, IEEE*, Sergio Amedeo Pignari , *Fellow, IEEE*, and Johannes Wolf, *Senior Member, IEEE*

Abstract—This work introduces a novel method to include the passive structure of a printed circuit board into an infinitesimal dipole model that is reconstructed from near-field measurement data. Specifically, the proposed approach enables the construction of equivalent models that include dipole sources, substrate, and perfect electric conductor plane. The electromagnetic near-fields of the infinitesimal dipoles in this configuration are estimated through an adaptation of the *partial image expansion* technique. The proposed method has the capability to provide accurate results for a wide variety of configurations. Furthermore, it can be easily incorporated into existing dipole array optimization workflows with minimal added computational complexity.

Index Terms—Infinitesimal dipole model, method of images, near-field scanning, printed circuit boards (PCB), radiated fields.

I. INTRODUCTION

NEAR-FIELD techniques are gaining increasing attention for electromagnetic compatibility (EMC) precompliance and compliance assessment. As demonstrated by [1], near-field probes can function as measurement instruments to identify radiated emissions, or as injection tools for immunity examination in frequency [2], [3] and time domain [4]. Specifically, near-field probes are widely employed to map the field distribution above a printed circuit board (PCB) to identify emission sources [3].

Data-driven radiation models that are based on near-field measurements are extremely valuable for early-stage EMC design and the subsequent testing. These models can be particularly useful when dealing with devices with limited internal space, where PCBs are closely stacked and near-field coupling between the PCB parts is the main cause for interference. Small satellites, commonly referred to as CubeSats, are examples of such devices.

Manuscript received 15 May 2023; revised 14 September 2023; accepted 7 October 2023. Date of publication 26 October 2023; date of current version 13 December 2023. This work was supported by the European Space Agency (ESA-ESTEC) under Grant ESA RFP/3-17397/21/NL/GLC/my. (*Corresponding author: Tomas Monopoli.*)

Tomas Monopoli, Xinglong Wu, Flavia Grassi, and Sergio Amedeo Pignari are with the Department of Electronics, Information and Bioengineering, Politecnico di Milano, 20133 Milano, Italy (e-mail: tomas.monopoli@polimi.it; xinglong.wu@polimi.it; flavia.grassi@polimi.it; sergio.pignari@polimi.it).

Johannes Wolf is with the Power Systems, EMC and Space Environment Division, European Space Technology Center, European Space Agency, 2201 AZ Noordwijk, The Netherlands (e-mail: johannes.wolf@esa.int).

Color versions of one or more figures in this article are available at <https://doi.org/10.1109/TEMC.2023.3325242>.

Digital Object Identifier 10.1109/TEMC.2023.3325242

In the EMC sector, the most prevalent approach involves constructing an equivalent radiated emission model of the device under test (DUT). In particular, the infinitesimal dipole model, which is grounded in multipole expansion theory, stands out as the preferred choice [5], [6]. This method represents the emitting sources with an array of infinitesimal dipoles, such that the emitted fields of the model coincide with measurements at the measurement points.

From an EMC modeling view point, a PCB can be seen as consisting of the following three main parts: 1) the radiating elements, 2) the dielectric substrate, and 3) the ground plane. The radiated emissions from such a configuration can be adequately approximated by an array of infinitesimal dipoles in free space. For example, this basic equivalent model, which solely consists of the dipole sources, is effective for predicting near-field to far-field radiation patterns. Nonetheless, the prevalent approach incorporates also the ground plane into the equivalent model, representing it as a perfect electric conductor (PEC) plane. This allows for any fringing and scattering effects from the ground to be included in the solution when the equivalent model is simulated by a commercial solver. In this setup, the fields generated by dipole sources are estimated by employing the method of images and the dipole array is optimized using these field expressions [7], [8]. For simplicity, the equivalent model made up of dipole sources and conductor plane is hereafter referred to as PEC model.

While the PEC model is generally effective, there has been some interest in extending it to include the PCB dielectric substrate. This approach was first introduced in [9] and termed the dipole-dielectric conducting plane (DDC) model. The rationale for incorporating the substrate is twofold. On the one hand, dielectric properties should be included as they are crucial for device performance [10]. On the other hand, including the substrate increases model versatility. Notably, the PEC model performs poorly when placed in a closed environment, where the lack of substrate causes a nonnegligible shift of the resonance frequencies. This issue has been comprehensively addressed in [11], where, conversely, the DDC model demonstrated robust performance even in such conditions. Furthermore, the equivalent sources in a DDC model are more likely to accurately represent the true physical sources on the PCB, as they do not need to account for the dielectric's scattering effects.

Despite these advantages, the DDC model has seen limited diffusion in the literature, while the PEC model remains the standard. This can largely be attributed to the lack of closed-form solutions for the electromagnetic (EM) fields generated by a dipole in a heterogeneous environment that includes a PEC plane, substrate, and air [12]. This leads many researchers and engineers to opt for the more tractable PEC model, despite its limitations. In their study [9], the authors addressed this challenge by developing exact analytical solutions exploiting the structure’s natural symmetry in cylindrical coordinates. However, they also pointed out numerical issues, such as stability problems related to improper integrals with ill-conditioned kernel functions. Moreover, their solutions are restricted to flat dipoles lying in the xy -plane, limiting the applicability for configurations that should ideally include both flat magnetic dipoles and normal electric dipoles [13]. An alternative approach, introduced in [10], employs an effective permittivity constant ϵ_{eff} in a virtual uniform medium to facilitate field estimations. While easier to implement, this strategy introduces an additional variable into the optimization process. Furthermore, the optimized ϵ_{eff} is only applicable to specific dipole arrangements and probe heights.

In this work, a novel approach based on the “partial image expansion” method is presented. This method ensures a good estimation of the EM near-fields radiated by dipole sources situated over a PEC-backed substrate, thus supplying new constituting equations to the DDC model. Notably, the method maintains its accuracy regardless of the dipole’s distance from the substrate or its orientation and it is applicable to both electric and magnetic dipoles. The primary aim of this article is to simplify the construction of the DDC model, a goal that is achieved by demonstrating that the application of partial image expansion allows for straightforward recalibration of the Green’s matrix. This can be readily incorporated into existing optimization and search algorithms that are designed for constructing equivalent dipole arrays. Finally, it is shown that no loss in accuracy occurs when transitioning from a PEC model to the new DDC model.

The rest of this article is organized as follows. In Section II, the basic principles of partial image expansion for estimating the position and intensity of the image dipoles are presented. In Section III, the procedure is extended to secondary-field prediction, i.e., H field of electric dipoles and E field of magnetic dipoles. Section IV explains how the proposed method can be integrated in a typical dipole optimization procedure. In Section V, the method is validated versus full-wave simulation and compared versus previous approaches. Application examples are presented in Section VI and compared with the reference models. Finally, Section VII concludes the article.

II. ADAPTED PARTIAL IMAGE EXPANSION

In order to build the infinitesimal dipole model, multiple measurements are usually taken with near-field probes on a flat plane over the DUT. EM fields are commonly measured in the reactive near field where they are mostly nonradiating. Instead, the field energy is stored in pockets close to the surface of the device and only a negligible portion is radiated away. It follows

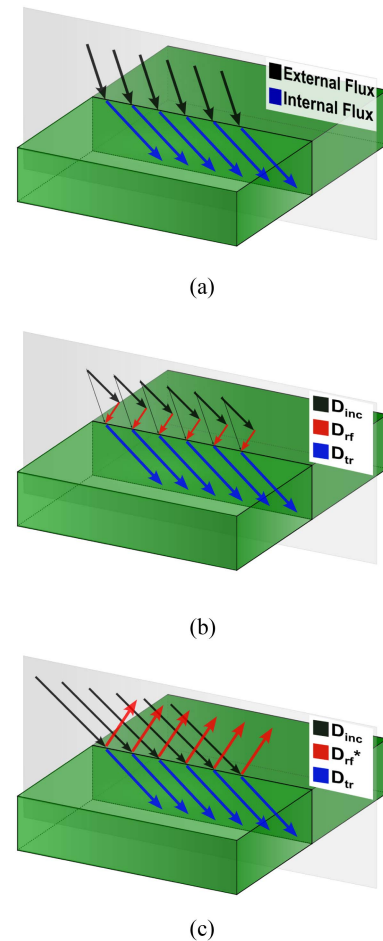


Fig. 1. Static electric flux density at a boundary. (a) Classical representation. (b) Deconstruction of the electric flux density outside the substrate. (c) Equivalent setup with incident, reflected, and transmitted components.

that the EM fields in this region resemble the behavior of static fields. Hence, a quasi-static approximation can be entertained, which enables the E and H fields to be considered independent of one another, i.e., mutual interactions can be neglected.

Under the quasi-static hypothesis, the “partial image expansion” method firstly expounded in [14] is here adapted to infinitesimal dipole sources. The method is based on the field decomposition in *incident*, *reflected*, and *transmitted* components. Hence, the following section will preliminary demonstrate how a unique set of these components can be introduced to represent an arbitrary static field in the presence of a boundary (see Fig. 1). Then, an alternative approach (w.r.t. [14]) will be introduced to determine the images of an arbitrary volume current source, resulting in simple expressions for the image positions and amplitudes of an arbitrary infinitesimal dipole.

A. Preliminary Considerations

The objective of this section is to show that there exists a unique equivalent representation based on incident, reflected, and transmitted components for an arbitrary static field. Without loss of generality, the electric flux density will be considered in

the following, but the results easily extend to the other field quantities.

Starting from the classical representation of the electric flux density at the boundary between air and a dielectric, see Fig. 1(a), the external field can be decomposed into the sum of two constituting components, the first of the two being parallel to it. This is shown in Fig. 1(b), where the external field vector is substituted by the composition of the incident field, D_{inc} , and the reflected field, D_{rf} . As long as the only constraint is that the transmitted field, D_{tr} in Fig. 1(b), is parallel to the incident field, D_{inc} , there is an infinite number of field pairs decomposing the incident field. In order for the pair to be unique, an extra constraint on the conservation of the total field is enforced, as

$$\|D_{inc}\| = \|D_{rf}\| + \|D_{tr}\| \quad (1)$$

where $\|\cdot\|$ denotes vector magnitude.

Typically, when considering the EM waves, the reflected component is directed away from the boundary surface in opposition to the incident wave. However, because the permittivity of the substrate is generally larger than the air permittivity, the reflected field D_{rf} is pointing toward the surface boundary rather than back outward [see Fig. 1(b)]. In order to preserve the analogy with the EM waves, the opposite reference system is chosen with a reflection vector pointing outward. Given this choice, the reflection coefficient, defined as

$$\Gamma = \|D_{rf}\|/\|D_{inc}\| \quad (2)$$

will assume negative values. It follows from (1) and (2)

$$\|D_{tr}\| = (1 - \Gamma)\|D_{inc}\|. \quad (3)$$

Given that the incident and transmitted components are parallel by design of the external field decomposition, from (1) and (3) and the boundary conditions of static fields, one can follow the procedure in [14] to obtain

$$\theta_{inc} = \theta_{tr} = \theta_{rf} \quad (4)$$

$$\Gamma = \frac{\epsilon_1 - \epsilon_2}{\epsilon_1 + \epsilon_2} \quad (5)$$

where ϵ_1 is the permittivity of the external medium (usually air) and ϵ_2 the permittivity of the substrate, while θ_{inc} , θ_{tr} , and θ_{rf} denote the incidence, transmission, and reflection angles, respectively. Equation (5) can be easily rewritten for the magnetic flux density, by simply replacing the dielectric permittivity constant with the magnetic permeability one. In many applications, the substrate does not exhibit magnetic properties, therefore, the reflection coefficient Γ for the magnetic flux density is usually null.

B. Image Position and Amplitude

Starting from the field decomposition presented in the previous section [14], a novel approach for the derivation of image amplitude and position is here presented.

Let us consider the case of an arbitrary infinitesimal source over a substrate with a PEC ground backing. Applying the decomposition described in Section II-A and considering that the PEC surface has a reflection coefficient of -1 , the emitted

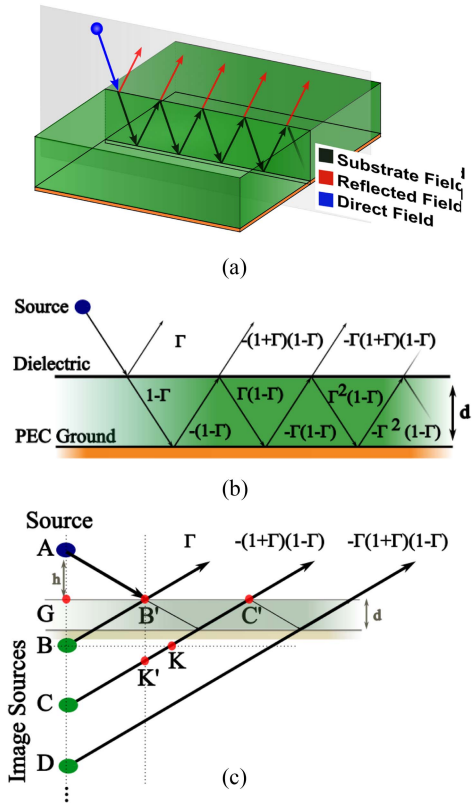


Fig. 2. Equivalent configurations. (a) Single flux line interacting with the substrate, (b) bounce diagram for the single flux line. Here, the intensity of the flux component is calculated after every reflection, and (c) equivalent configuration with image sources in a uniform medium.

field can be represented as in Fig. 2(a). At each interaction with the boundary, the reflected and transmitted field components are evaluated by using the properties of the reflection coefficient. The results are summarized and illustrated in the bounce diagram in Fig. 2(b). As the reflected field components are all parallel, a uniform space with multiple image sources can be constructed such that the total field above the dielectric is the same as in Fig. 2(b). This is shown in Fig. 2(c). In order for the setup in Fig. 2(c) to be a valid equivalent of the one in Fig. 2(a), the position and amplitude of each image should be independent of the particular field line considered from the source, i.e., image positions and values should be independent of the incidence angle. The expressions of image position and amplitude derived in the following will prove such a property.

1) *Image Position*: The positions of the partial images are determined using some simple trigonometry. Indeed, if h is the height of the arbitrary source above the dielectric [see: Fig. 2(c)], the isosceles triangle $AB'B$ results in

$$L_{B-G} = L_{A-G} = h \quad (6)$$

where L_{X-Y} indicates the distance between points X and Y. Therefore, the position of the first image is set to $-h$ below the interface surface. Also, the triangles $B'C'K'$ and BCK are similar and $L_{B'-C'}$ and L_{B-K} are equal by construction. It

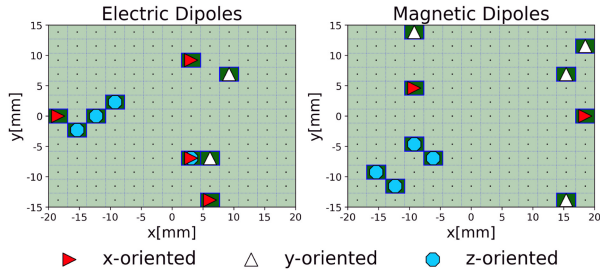


Fig. 3. Random electric dipole array and random magnetic dipole array. The value of the moments are reported in Table I.

TABLE I
DIPOLE MOMENTS

Magnitude (X m)	Phase (degrees)
8.54×10^{-7}	48
2.55×10^{-7}	13
3.00×10^{-7}	63
1.22×10^{-6}	52
7.39×10^{-7}	13
7.62×10^{-7}	20
6.39×10^{-7}	82
1.55×10^{-7}	14
8.86×10^{-7}	2
8.11×10^{-7}	54

follows that

$$L_{BC=} = L_{B'-K'} = 2d \quad (7)$$

where d is the thickness of the dielectric. Accordingly, the distance between the first and second image is equal to $2d$, that is twice the thickness of the board. The same procedure can be applied for all subsequent reflections, so that each new image is placed at a distance $2d$ from the previous. Hence, the position r_n of the n th image in the expansion can be written as

$$r_n = -h - 2n \cdot d \quad (8)$$

with $n = 0, 1, \dots$

2) *Image Amplitude*: Amplitudes of the images are set equal to the amplitudes of the reflected field component in Fig. 2(b). Indeed, the original field is recovered by summing the incident component with all reflections (as a consequence of the definition of Γ with the original D_{rf}). Therefore, the amplitude of the n th image can be cast as

$$\begin{aligned} Q_0 &= \Gamma \rho \\ Q_n &= -\Gamma^{n-1} (1 - \Gamma^2) \rho \end{aligned} \quad (9)$$

where ρ is an arbitrary volume current density, i.e., the original source, and Q_i is the volume current density of the i th image.

The values in Fig. 2(b) are obtained by the following considerations. First, at the boundary with a PEC material, the field is completely reflected [14], [15]. Second, it follows from (5) that the reflection coefficient of the field incident to the boundary from inside the substrate is $-\Gamma$. Equation (9) is in general applicable to an arbitrary volume density charge ρ and the application to infinitesimal dipoles is straightforward [15]. Also, the above procedure easily extends to the magnetic flux density vector.

To validate the proposed model, the obtained field prediction is compared versus the prediction obtained by the commercial solver HFSS [16]. A substrate with thickness 0.4 mm of FR4 epoxy material ($\epsilon_r = 4.4$) and backed with a PEC plane is considered. The substrate size is set to 100×100 cm. An arbitrary dipole array is considered for electric and magnetic dipoles as shown in Fig. 3. The dipole height over the substrate surface is set to 3 mm. Indeed, it is necessary to introduce a gap between the dipoles and the substrate surface in order to retain the radiation properties of infinitesimal dipoles. The field is acquired at 3 cm from the substrate. The magnitude and phase

of dipole moments at 1 GHz are chosen at random and collected in Table I, with units in V/m and A/m for electric and magnetic dipoles, respectively. In practice, the contribution of the image sources becomes negligible after the first 7 or 8 terms. In the following, all partial image expansions are truncated after 15 terms for good measure. The comparison between full-wave simulation (HFSS) and the proposed infinitesimal dipole model demonstrates an accurate reconstruction of the field distribution. A 2-D plot of the field's numerical estimation versus HFSS simulation result is shown in Fig. 4 and a detailed view for $y = 0$ mm is given in Fig. 5 to allow a more direct comparison.

III. SECONDARY FIELD PREDICTION

In the previous section, the accuracy of the partial image method in predicting the primary field emitted by infinitesimal dipoles was proven, where ‘‘primary field’’ refers to the E field of electric dipoles and H field of magnetic dipoles. In this section, a methodology ensuring a good estimate of also the secondary field (i.e., H field of electric dipoles and E field of magnetic dipoles) will be presented. Indeed, knowledge of the secondary field may contribute to development of accurate dipole equivalent models. For instance, in [9], the magnetic field of flat electric dipoles was used to reproduce the target tangential H field. More in general, if the equivalent dipole includes both electric and magnetic dipoles, the overall magnetic and electric field is given by the superposition of the main and secondary field components.

In the previous section, the primary fields were estimated as if the secondary fields were not present. In the same way, here, also the secondary fields are estimated assuming no influence from the primary fields. This leads to a partial image expansion similar to that in Section II in which the role of the electric permittivity ϵ and magnetic permeability μ is swapped in the definition of the reflection coefficient

$$\Gamma = \begin{cases} (\epsilon_1 - \epsilon_2) / (\epsilon_1 + \epsilon_2) & \text{for magnetic dipoles} \\ (\mu_1 - \mu_2) / (\mu_1 + \mu_2) & \text{for electric dipoles} \end{cases} \quad (10)$$

However, the secondary fields predicted by this approach poorly compare to HFSS simulations, since the above assumption is too simplistic for secondary field prediction. Hence, to achieve a better prediction, a certain degree of dependence, denoted as ξ in the following, needs to be considered. The value of ξ can range from $\xi = 0$ to $\xi = 1$, which denote total independence

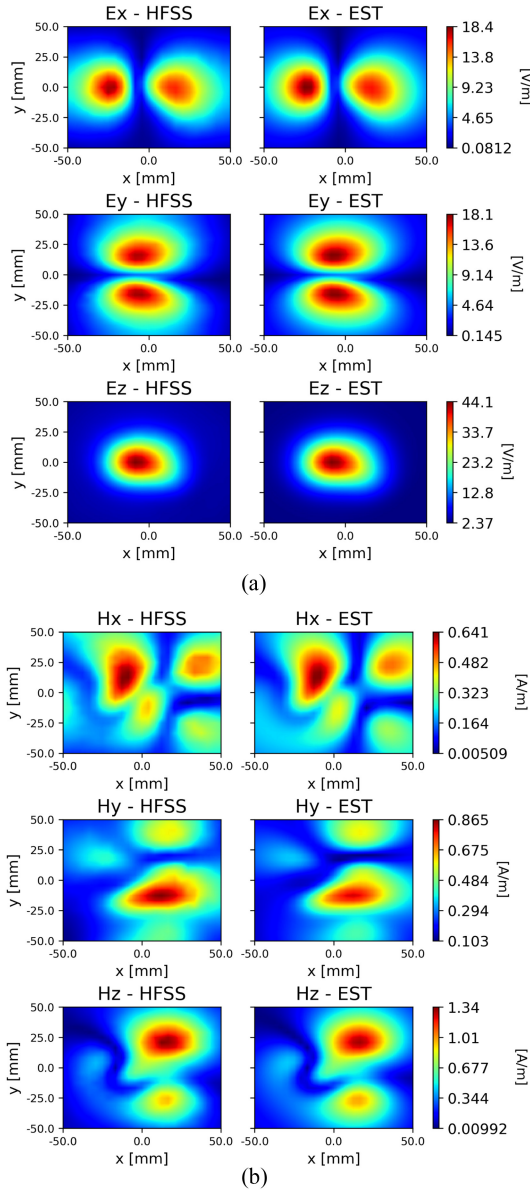


Fig. 4. Comparison of HFSS simulation (HFSS) and the numerical estimation (EST) of the primary fields emitted by the random dipole array in Fig. 3. (a) E field emitted by the random array of electric dipoles in Fig. 3. (b) H field emitted by the random array of magnetic dipoles in Fig. 3.

and full dependence, respectively, of the secondary field. The case $\xi = 0$ corresponds to the abovementioned assumption of independence of the secondary field from the primary field; see (10). In the case $\xi = 1$, the secondary field is fully determined by the primary field (even if it does not influence it). To investigate this latter case, we enforce Maxwell's equations for lossless media, i.e.,

$$\begin{aligned} E &= \frac{1}{j\omega\epsilon} \nabla \times H \\ H &= -\frac{1}{j\omega\mu} \nabla \times E \end{aligned} \quad (11)$$

where ω is the angular frequency.

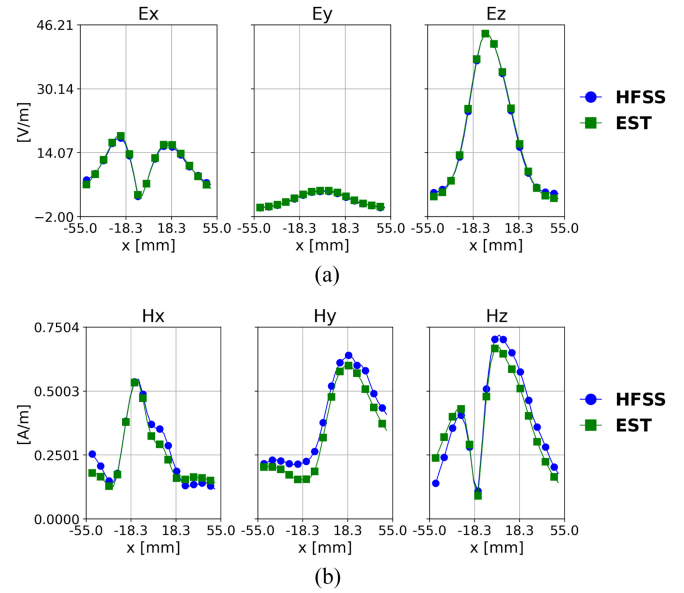


Fig. 5. Comparison of HFSS simulation (HFSS) and the numerical estimation (EST) of the primary fields emitted by the random dipole array in Fig. 3. (a) E field emissions (random array of electric dipoles) in the x direction, for $y = 0$. (b) H field emissions (random array of magnetic dipoles) in the x direction, for $y = 0$ mm.

The optimum value of ξ can be searched for empirically by interpolating between the previous extreme cases (10) and (11). Taking a magnetic dipole as an example, the estimated electric field can be written as

$$E = E_{ind} + \xi \cdot [E_{dep} - E_{ind}] \quad (12)$$

where E_{ind} denotes the electric field estimated according to (10), i.e., $\xi = 0$; and E_{dep} is the electric field estimated according to (11), i.e., $\xi = 1$.

It can be observed empirically, that the interpolation coefficient depends on the dipole orientation. A good approximation of the secondary field was found by setting $\xi = 0.5$ for flat dipoles (parallel to PCB planes) and $\xi = 0.95$ for normal dipoles (perpendicular to PCB planes). These values were tested for different substrate material and thickness as well as different heights from the board surface and a range of frequencies up to 10 GHz. In all cases, field predictions were affected by a small relative error (under 5% with respect to the field maximum). Thanks to field duality, the same interpolation coefficients are valid for both E and H dipoles.

The comparison between secondary-field prediction obtained by the proposed model and by HFSS simulation is shown in Figs. 6 and 7. For the HFSS simulation, magnetic dipoles were modeled as incident Hertzian-dipole waves in the points of interest, whereas electric dipoles were represented by flat rectangles set to PEC boundary and excited by a current source [17].

IV. INTEGRATION INTO DIPOLE MODELING WORKFLOWS

The developed method can be simply integrated into the workflow for equivalent dipole array reconstruction. First, closed-form expressions for the EM fields generated by an infinitesimal

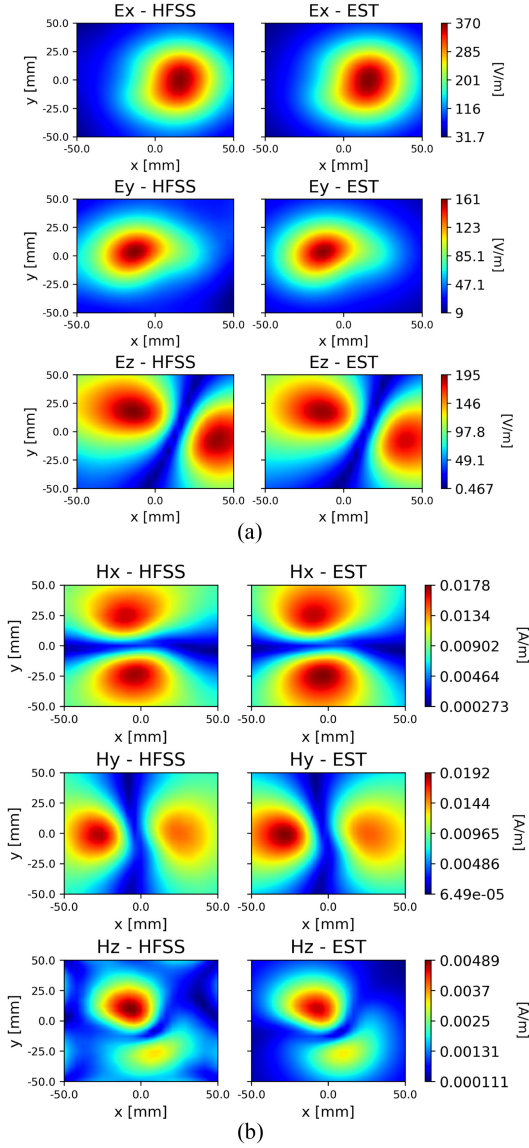


Fig. 6. Comparison of HFSS simulation (HFSS) and the numerical estimation (EST) of the secondary fields emitted by the random dipole array in Fig. 3: (a) E field emitted by the random array of magnetic dipoles in Fig. 3, (b) H field emitted by the random array of electric dipoles in Fig. 3.

dipole in uniform media should be considered [12]. Establishing a linear relationship between the dipole moments and the resultant EM field values is possible by fixing the dipole position and orientation [18]. In practice, the field is evaluated at discrete points, yielding a matrix representation of the field

$$\mathbf{F} = \mathbf{G} \cdot \mathbf{M}. \quad (13)$$

Here, \mathbf{F} represents the field values (either E or H) at the points of interest, \mathbf{M} is the dipole moments, and \mathbf{G} is the Green Matrix for a uniform space.

Then, to incorporate the PEC-backed substrate into the model, the EM fields generated by the dipole sources are estimated using the methods developed above. For each term in the expansion, an expression akin to (13) is obtained

$$\mathbf{F}^{(k)} = \mathbf{G}^{(k)} \cdot \mathbf{M}^{(k)} \text{ for } k = 0, 1, \dots, K \quad (14)$$

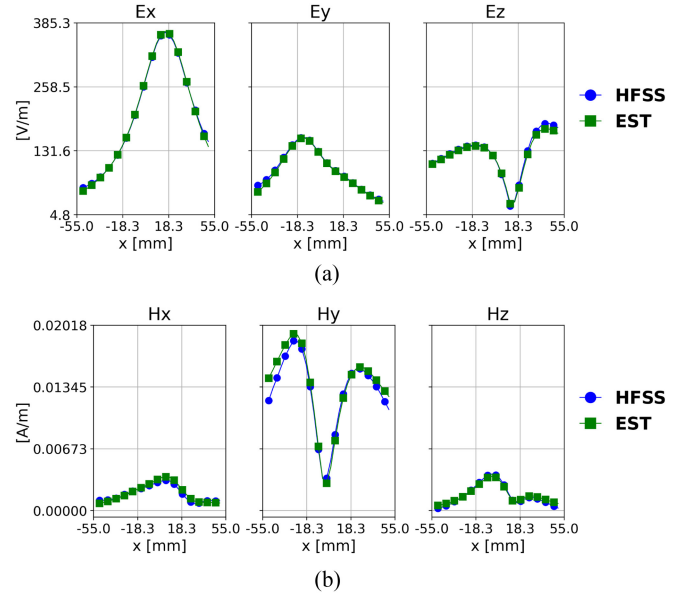


Fig. 7. Comparison of HFSS simulation (HFSS) and the numerical estimation (EST) of the secondary fields emitted by the random dipole array in Fig. 3. (a) E field (random array of magnetic dipoles) in the x direction, for $y = 0$ mm. (b) H field emissions (random array of electric dipoles) in the x direction, for $y = 0$ mm.

where $\mathbf{M}^{(k)}$ denotes the k th dipole moments, $\mathbf{G}^{(k)}$ is the Green Matrix for uniform space of the dipoles of the k th term, $\mathbf{F}^{(k)}$ is the field contribution of the k th term, and K is the total number of terms considered in the expansion. Dipole moments $\mathbf{M}^{(k)}$ are proportional to the source moments as in (9), hence

$$\mathbf{F}^{(k)} = Q_k \mathbf{G}^{(k)} \cdot \mathbf{M} \text{ for } k = 0, 1, \dots, K. \quad (15)$$

By the superposition principle, the contributions of each term are summed to obtain an equivalent formulation of (13)

$$\mathbf{F} = \tilde{\mathbf{G}} \cdot \mathbf{M} \quad (16)$$

where $\tilde{\mathbf{G}}$ is defined as the sum of all $Q_k \mathbf{G}^{(k)}$ terms and is a near-field approximation for the Green Matrix of the nonuniform medium under consideration. Importantly, the expansion's image dipoles' positions and orientations are intrinsically tied to the corresponding attributes of their originating dipole sources. Consequently, when optimizing the configuration of the dipoles, the only parameters required for consideration are the position and orientation of the initial dipoles. In other words, both \mathbf{G} and $\tilde{\mathbf{G}}$ are dependent on these same parameters. Hence, integrating the proposed model into a traditional source reconstruction workflow, to directly include the effects of the substrate and PEC, only requires the replacement of (13) with (16). The process can further be adapted to accommodate secondary dipole fields, given that the equations outlined in Section III also result in a partial image expansion, with the only modification being to the respective dipole moments.

V. COMPARISON WITH OTHER MODELING APPROACHES

In this section, the proposed method is compared with two other approaches present in the literature: 1) the traditional image

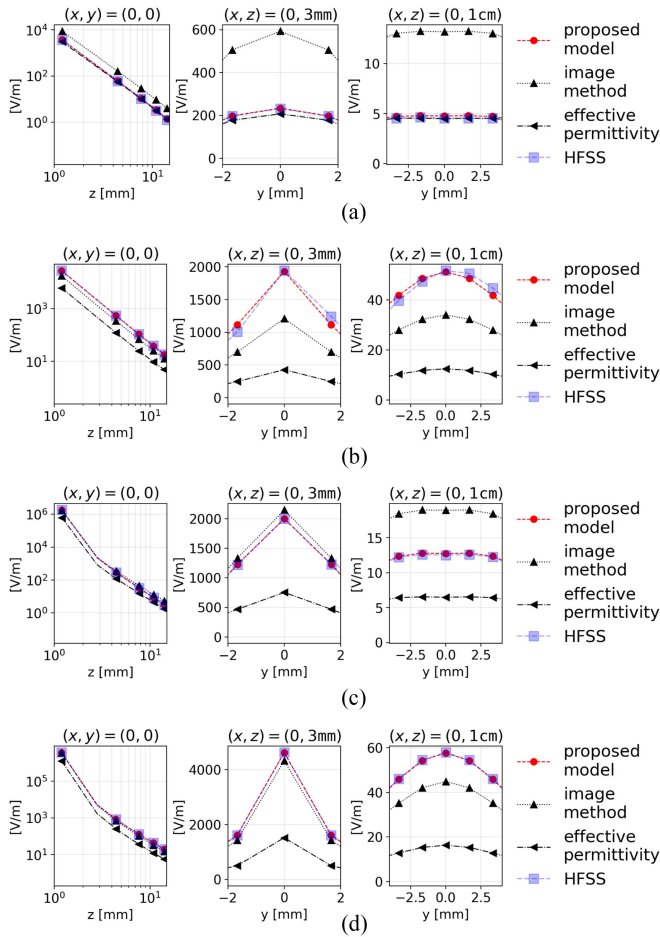


Fig. 8. Comparison between different dipole models and HFSS simulation in different configurations. (a) Flat dipole at $20 \mu\text{m}$ above the surface. (b) Vertical dipole at $20 \mu\text{m}$ above the surface. (c) Flat dipole at 1 cm above the surface. (d) Normal dipole at 1 mm above the surface.

method 2) and the effective permittivity method. The traditional image model only considers the PEC plane and neglects the presence of the substrate. This results in a single dipole image placed symmetrically with respect to the PEC plane. In addition to considering the PEC plane, the *effective permittivity method* replaces the actual nonhomogeneous medium (substrate and air) with a homogeneous medium exhibiting an equivalent permittivity ϵ_{eff} [10]. The value of the equivalent permittivity ϵ_{eff} is dynamically determined together with dipole orientation and amplitude by a global search algorithm [10].

In order to compare the three approaches, a single dipole is considered, placed at the center of a substrate with thickness 5.4 mm of FR4 epoxy material. A dipole moment of $1 \times 10^{-5} \text{ V} \cdot \text{m}$ is considered at a frequency of 1 GHz for different heights and orientations of the dipole. The obtained results are compared versus HFSS simulation, taken as reference solution, in Fig. 8. Each row of Fig. 8 contains three subplots, the leftmost compares E field predictions along the z direction, the middle plot and the rightmost compare E fields predictions along the y direction at two different heights above the board: $z = 1 \text{ mm}$ and $z = 1 \text{ cm}$. Since for the effective permittivity method, the choice

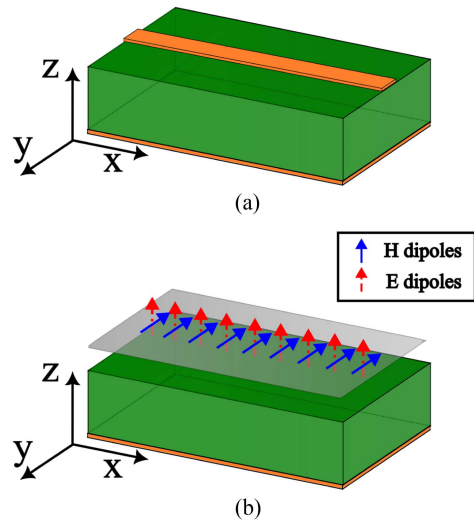


Fig. 9. (a) Original reference fixture and (b) equivalent DDC model.

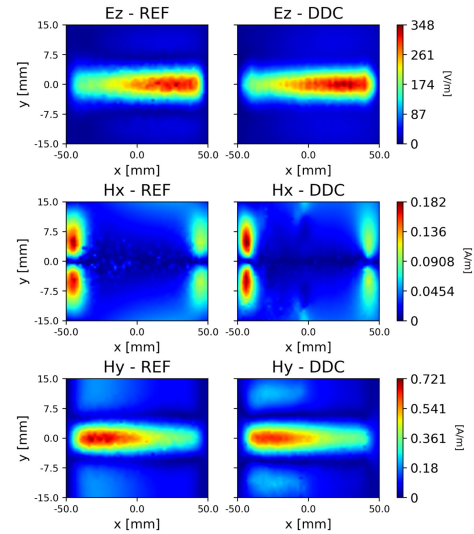


Fig. 10. Simple Strip Structure. Fieldmap comparison between the HFSS reference model (REF) and the DDC model (DDC) at 6 mm height.

of ϵ_{eff} introduces an extra degree of freedom, the permittivity parameter used for the simulations was tuned so as to perfectly predict the electric field at $z = 1 \text{ cm}$ of a flat electric dipole set at $20 \mu\text{m}$ from the surface. This setup is the one analyzed in Fig. 8(a) and indeed a perfect match is shown between the effective permittivity model and the HFSS simulation.

The comparison shows that the proposed method, based on partial image expansion, yields predictions in appreciable agreement with HFSS simulation in all test cases. The procedure employing the effective permittivity [10] assures a perfect match in the test case for which ϵ_{eff} is tuned [see Fig. 8(a)], but it does not retain the same accuracy in the other cases. As a matter of fact, ϵ_{eff} is highly correlated to dipole orientation, and therefore, the determination of ϵ_{eff} is necessarily an integral part of the dipole optimization algorithm. Eventually, it is worth noting that if the inspection height is relatively close to the dipole source,

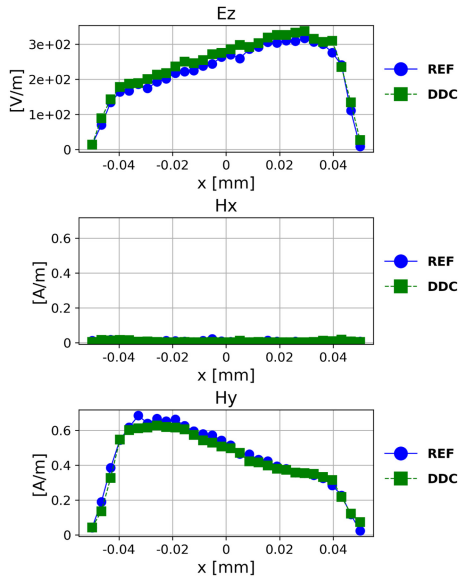


Fig. 11. Comparison between the HFSS reference model (REF) and the DDC model (DDC) at 6 mm height at $y = 0$ mm.

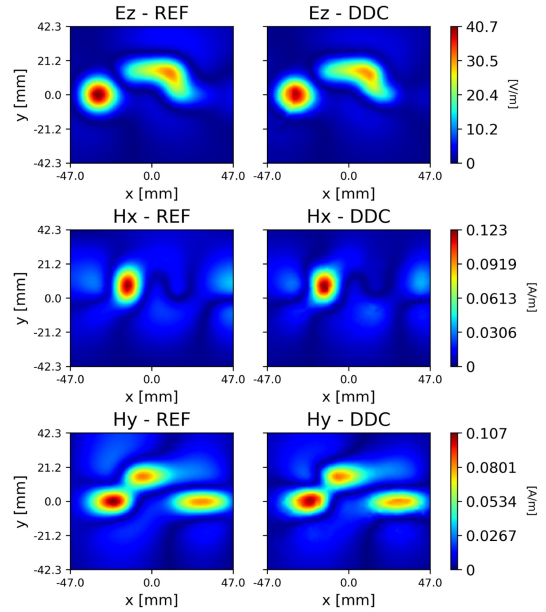


Fig. 13. Fieldmap comparison between the HFSS reference model (REF) and the DDC model (DDC) at 1.2 cm height.

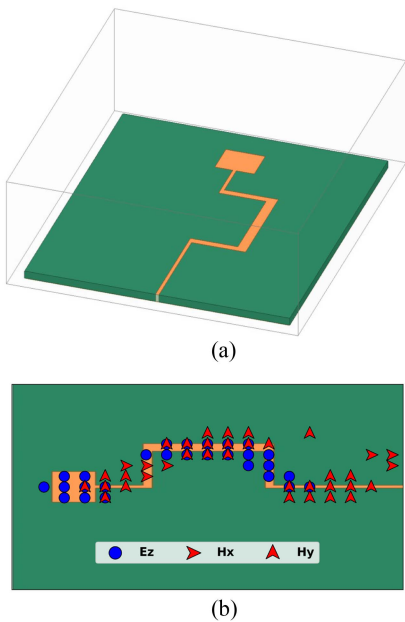


Fig. 12. Bent strip terminating in a patch. (a) HFSS model. (b) Equivalent dipole array at 1 mm above the substrate surface. E_z : electric dipoles oriented along z ; H_x : magnetic dipoles oriented along x ; H_y : magnetic dipoles oriented along y .

also the traditional image method (neglecting the substrate) can yield good field approximation; see Fig. 8(c) and (d), most likely because the *direct* component of the field is dominant at this height and the substrate effect is less evident.

VI. APPLICATION EXAMPLES

In this section, the developed technique will be implemented in two test cases. First, a single trace with 1 mm width on a PCB is considered [see Fig. 9(a)] and developed in the HFSS.

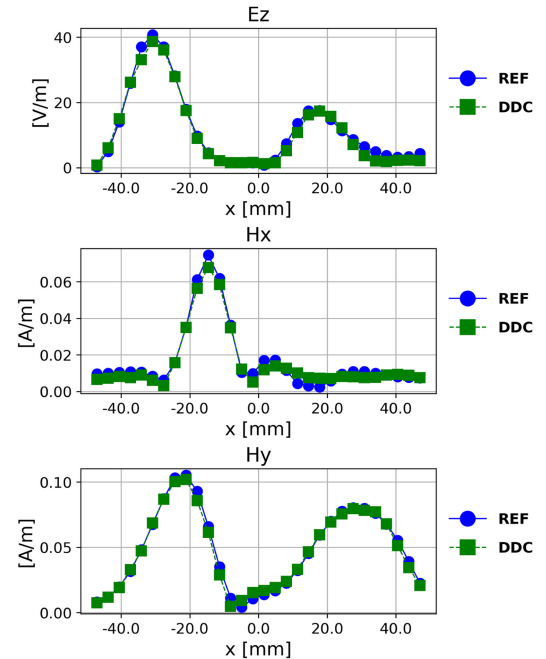


Fig. 14. Comparison between HFSS reference model (REF) and the DDC model (DDC) at 1.2 cm height at $y = 0$ mm.

The equivalent dipole model is built considering the presence of a PEC-backed substrate with the following characteristics: substrate material FR4 epoxy ($\epsilon_r = 4.4$), substrate thickness 0.7 mm, null trace thickness (constructed as PEC sheet in HFSS), PCB dimensions 10 cm \times 3 cm. E and H fields are sampled on a measurement plane 5 mm above the substrate surface. The DDC model is built by placing normal electric dipoles and tangential magnetic dipoles above the dielectric in place of the trace, as

shown in Fig. 9(b). For this simple case, the positions of the dipoles are chosen by inspecting the original structure as shown, e.g., in [[19], Figs. 6 and 8]. Finally, the Green matrix is obtained following the procedure described in Section IV and the optimal dipole moments are determined via its pseudoinverse [7], [13]. The original structure and equivalent model fields are compared in Figs. 10 and 11 showing a good agreement. As a more complex example, a bent strip-line ending with a patch is considered [see Fig. 12(a)] with the following properties: length 8 cm, a strip width of 9 cm, patch size of 1 cm \times 1.2 cm and an FR4 epoxy substrate with permittivity $\epsilon_r = 4.4$, thickness 2.4 cm and size 9 cm \times 8.1 cm. The z component of the electric field and the tangential components of the magnetic field are measured on a plane 1 cm from the dielectric surface. By analyzing these field components, an optimal array of dipoles is selected as shown in Fig. 12(b). For this application, a custom method was employed to find optimal positions and orientations. However, it is worth mentioning that partial image expansion can be easily integrated in the same way into any other technique used in the literature, such as differential evolution algorithms [20], [21], [22], quantum particle swarm optimization [23], [24], image processing techniques [25], iterative techniques [26], or methods based on neural networks [27]. Finally, the dipole moments are obtained again by calculating the pseudoinverse of the Green matrix. Alternatively, if no phase information is available, the Levenberg–Marquardt algorithm or other nonlinear optimization methods can be employed [28], [29]. The original reference model and the equivalent DDC model are compared at a height of 1.2 cm. The comparison is illustrated in Figs. 13 and 14, showing an excellent agreement.

These application examples and relative figures confirm the effectiveness of the approach for the creation of an accurate DDC model.

VII. CONCLUSION

In this work, a versatile dipole-based model exploiting partial image expansion has been introduced. The proposed methodology has been proven to generate accurate predictions of both the primary and secondary fields radiated by infinitesimal dipoles placed over a PEC-backed substrate. Furthermore, the model remains accurate for both electric and magnetic dipoles irrespective of their orientation and height above the substrate.

The practical application of this method requires merely that the substrate surface and PEC plane fall within the reactive near field region of the dipole source, a condition generally easily satisfied in constructing dipole models. This lenient requirement broadens the method applicability across various scenarios, augmenting its practical utility. Also, the ease of integrating the partial image expansion method into traditional source reconstruction workflows enhances its utility, as it can be directly incorporated by simply updating the Green's function matrix. To prove the effectiveness of the proposed method, two application examples have been presented: 1) a simple flat trace and 2) a bent trace terminating in a patch. The results prove the accuracy of the proposed approach in building DDC models for different boards with different properties.

The proposed methodology provides a straightforward solution to incorporate the passive components of a PCB in the equivalent model, which in turn enables more complex simulation.

REFERENCES

- [1] E.-X. Liu, W.-J. Zhao, B. Wang, S. Gao, and X.-C. Wei, "Near-field scanning and its EMC applications," in *Proc. IEEE Int. Symp. Electromagn. Compat. Signal/Power Integrity*, 2017, pp. 327–332.
- [2] X. Wu, F. Grassi, G. Spadacini, S. A. Pignari, U. Paoletti, and I. Hoda, "Investigation of semi-rigid coaxial test probes as RF injection devices for immunity tests at PCB level," *IEEE Access*, vol. 8, pp. 147919–147929, 2020.
- [3] D. Baudry, C. Arcambal, A. Louis, B. Mazari, and P. Eudeline, "Applications of the near-field techniques in EMC investigations," *IEEE Trans. Electromagn. Compat.*, vol. 49, no. 3, pp. 485–493, Aug. 2007.
- [4] X. Wu, F. Grassi, G. Spadacini, S. A. Pignari, U. Paoletti, and I. Hoda, "Test design methodology for time-domain immunity investigations using electric near-field probes," *IEEE Trans. Electromagn. Compat.*, vol. 64, no. 3, pp. 603–612, Jun. 2022.
- [5] S. M. Mikki and A. A. Kishk, "Theory and applications of infinitesimal dipole models for computational electromagnetics," *IEEE Trans. Antennas Propag.*, vol. 55, no. 5, pp. 1325–1337, May 2007.
- [6] I. V. Lindell, *Methods for Electromagnetic Field Analysis*. New York, NY, USA: Oxford Univ. Press, 1992.
- [7] D. W. P. Thomas, C. Obiekezie, and X. Tong, "Equivalent dipole models of electromagnetic emissions from near-field scanning," *IEEE Electromagn. Compat. Mag.*, vol. 4, no. 3, pp. 74–78, 3rd Quarter 2015.
- [8] Y. Vives-Gilbert, C. Arcambal, A. Louis, F. de Daran, P. Eudeline, and B. Mazari, "Modeling magnetic radiations of electronic circuits using near-field scanning method," *IEEE Trans. Electromagn. Compat.*, vol. 49, no. 2, pp. 391–400, May 2007.
- [9] X. Tong, D. W. P. Thomas, A. Nothofer, P. Sewell, and C. Christopoulos, "Modeling electromagnetic emissions from printed circuit boards in closed environments using equivalent dipoles," *IEEE Trans. Electromagn. Compat.*, vol. 52, no. 2, pp. 462–470, May 2010.
- [10] A. Ramanujan, Z. Riah, A. Louis, and B. Mazari, "Modeling the electromagnetic radiation of passive microwave components using a near-field scanning method," *IEEE Trans. Electromagn. Compat.*, vol. 52, no. 4, pp. 1056–1059, Nov. 2010.
- [11] X. Tong, "Simplified equivalent modelling of electromagnetic emissions from printed circuit boards," Thesis (University of Nottingham) (PhD), University of Nottingham, 2010.
- [12] J. Kong, *Electromagnetic Wave Theory, Ser. A. Wiley-Interscience Publication*. New York, NY, USA: Wiley, 1986.
- [13] Z. Yu, J. A. Mix, S. Sajuyigbe, K. P. Slattery, and J. Fan, "An improved dipole-moment model based on near-field scanning for characterizing near-field coupling and far-field radiation from an IC," *IEEE Trans. Electromagn. Compat.*, vol. 55, no. 1, pp. 97–108, Feb. 2013.
- [14] P. Silvester, "Tem wave properties of microstrip transmission lines," in *Proc. Inst. Elect. Eng.*, vol. 115, no. 1, pp. 43–48, 1968.
- [15] D. M. Pozar, *Microwave Engineering*. Hoboken, NJ, USA: Wiley, 2011.
- [16] "HFSS (High Frequency Structure Simulator) From ANSYS," [Online]. Available: <https://www.ansys.com/products/electronics/ansys-hfss>
- [17] P. F. Lopez, A. Ramanujan, Y. V. Gilbert, C. Arcambal, A. Louis, and B. Mazari, "A radiated emission model compatible to a commercial electromagnetic simulation tool," in *Proc. 20th Int. Zurich Sympo. Electromagn. Compat.*, 2009, pp. 369–372.
- [18] G. Lientschnig, "Multiple magnetic dipole modeling coupled with a genetic algorithm," in *Proc. ESA Workshop Aerosp.*, May 2012, pp. 2–8.
- [19] B. Wang, E.-X. Liu, W.-J. Zhao, and C. E. Png, "Reconstruction of equivalent emission sources for PCBs from near-field scanning using a differential evolution algorithm," *IEEE Trans. Electromagn. Compat.*, vol. 60, no. 6, pp. 1670–1677, Dec. 2018.
- [20] J. Li, X.-C. Wei, L. Gao, and Y.-F. Shu, "An effective equivalent radiation source based on near-field scanning for electromagnetic interference estimation," in *Proc. Asia-Pacific Int. Symp. Electromagn. Compat.*, 2017, pp. 315–317.
- [21] T.-H. Song, X.-C. Wei, J.-J. Ju, W.-T. Liang, and R.X.-K. Gao, "An effective EMI source reconstruction method based on phaseless near-field and dynamic differential evolution," *IEEE Trans. Electromagn. Compat.*, vol. 64, no. 5, pp. 1506–1513, Oct. 2022.

- [22] W.-J. Zhao, E.-X. Liu, B. Wang, S.-P. Gao, and C. E. Png, "Differential evolutionary optimization of an equivalent dipole model for electromagnetic emission analysis," *IEEE Trans. Electromagn. Compat.*, vol. 60, no. 6, pp. 1635–1639, Dec. 2018.
- [23] S. Mikki and A. Kishk, "Quantum particle swarm optimization for electromagnetics," *IEEE Trans. Antennas Propag.*, vol. 54, no. 10, pp. 2764–2775, Oct. 2006.
- [24] F.-P. Xiang, E.-P. Li, X.-C. Wei, and J.-M. Jin, "A particle swarm optimization-based approach for predicting maximum radiated emission from PCBs with dominant radiators," *IEEE Trans. Electromagn. Compat.*, vol. 57, no. 5, pp. 1197–1205, Oct. 2015.
- [25] Y. Vives-Gilabert, C. Arcambal, A. Louis, P. Eudeline, and B. Mazari, "Modeling magnetic emissions combining image processing and an optimization algorithm," *IEEE Trans. Electromagn. Compat.*, vol. 51, no. 4, pp. 909–918, Nov. 2009.
- [26] C. Wu, Z. Sun, Q. Huang, Y. Wang, J. Fan, and J. Zhou, "A method to extract physical dipoles for radiating source characterization and near field coupling estimation," in *Proc. IEEE Int. Symp. Electromagn. Compat. Signal Power Integr.*, 2019, pp. 580–583.
- [27] Y.-F. Shu, X.-C. Wei, J. Fan, R. Yang, and Y.-B. Yang, "An equivalent dipole model hybrid with artificial neural network for electromagnetic interference prediction," *IEEE Trans. Microw. Theory Techn.*, vol. 67, no. 5, pp. 1790–1797, May 2019.
- [28] A. Ramanujan, Z. Riah, A. Louis, and B. Mazari, "Computational optimizations towards an accurate and rapid electromagnetic emission modeling," *Prog. Electromagn. Res. B*, vol. 27, pp. 365–384, 2011.
- [29] W.-J. Zhao et al., "An effective and efficient approach for radiated emission prediction based on amplitude-only near-field measurements," *IEEE Trans. Electromagn. Compat.*, vol. 54, no. 5, pp. 1186–1189, Oct. 2012.



Tomas Monopoli received the double M.Sc. degrees (cum laude) in electrical engineering from the University of Politecnico di Milano, Milan, Italy and Politecnico di Torino, Turin, Italy, in 2020. He is currently working toward the Ph.D. degree in electrical engineering with the Department of Electronics, Information and Bioengineering, Politecnico di Milano.

In 2021, he was a Research Fellow with the European Space Agency (ESA), ESA/ESTEC, Noordwijk, the Netherlands. His research interests include

radiated emission testing, near field measurements, near-field probes, machine learning, and deep learning applied to EMC modeling.



Xinglong Wu (Member IEEE) received the double M.Sc. degrees from Xi'an Jiaotong University, Xi'an, China and Politecnico di Milano, Milan, Italy, in 2015, and the Ph.D. degree (summa cum laude) from Politecnico di Milano, in 2019, all in electrical engineering.

He is currently an Assistant Professor with the Department of Electronics, Information and Bioengineering, Politecnico di Milano. From March 2017 to June 2017, he was a Visiting Scientist with the Electromagnetics Group, Department of Information

Technology, Ghent University, Ghent, Belgium. From 2019 to 2020, he was a Postdoctoral Research Fellow with Politecnico di Milano. His research interests include distributed parameter circuit modeling, statistical techniques for electromagnetic compatibility (EMC), experimental procedures and setups for EMC testing, power electronics EMC, and system-level EMC.

Dr. Wu was the recipient of the International Union of Radio Science (URSI) Young Scientist Award from the 2020 URSI General Assembly and Scientific Symposium.



Flavia Grassi (Senior Member, IEEE) received the Laurea (M.Sc.) and Ph.D. degrees in electrical engineering from Politecnico di Milano, Milan, Italy, in 2002 and 2006, respectively.

She is currently a Full Professor with the Department of Electronics, Information and Bioengineering, Politecnico di Milano. From 2008 to 2009, she was a Research Fellow with the European Space Agency (ESA), ESA/ESTEC, Noordwijk, the Netherlands. Her research interests include theoretical and experimental characterization of EM interference via

lumped and distributed circuit modeling, characterization and development of measurement procedures and setups for EMC assessment of avionic, automotive, and power systems, and statistical techniques, EMC, and coexistence issues in power systems.

Dr. Grassi was the recipient of the International Union of Radio Science (URSI) Young Scientist Award in 2008, and IEEE Young Scientist Award at the 2016 Asia-Pacific Int. Symposium on EMC (APEMC), IEEE EMC Society 2016 and 2021 Transactions Prize Paper Award, and the Best Symposium Paper Award at the 2015 and 2018 APEMC.



Sergio Amedeo Pignari (Fellow, IEEE) received the Laurea (M.Sc.) and Ph.D. degrees in electronic engineering from Politecnico di Torino, Turin, Italy, in 1988 and 1993, respectively.

From 1991 to 1998, he was an Assistant Professor with the Department of Electronics, Politecnico di Torino. In 1998, he joined Politecnico di Milano, Milan, Italy, where he is currently a Full Professor of circuit theory and electromagnetic compatibility (EMC) with the Department of Electronics, Information, and Bioengineering. He served as the Chair

for the B.Sc. and M.Sc. Study Programmes in electrical engineering, term (2015–2020). He has authored or coauthored more than 220 papers published in international journals and conference proceedings. His research interests include EMC and include field-to-wire coupling and crosstalk, conducted immunity and emissions in multiwire structures, statistical techniques for EMC prediction, experimental procedures and setups for EMC testing, aerospace, automotive, energy, and railway industry sectors.

Dr. Pignari was a corecipient of the 2005, 2016, and 2021 IEEE EMC Society Transactions Prize Paper Award, and the recipient of IEEE EMC Society Technical Achievement Award in 2011. He is currently an Associate Editor for IEEE TRANSACTIONS ON ELECTROMAGNETIC COMPATIBILITY. From 2010 to 2015, he served as IEEE EMC Society Chapter Coordinator. From 2007 to 2009, he was the Chair of IEEE Italy Section EMC Society Chapter. He served as the Italian URSI Officer for Commission E (Electromagnetic Noise and Interference), term (2015–2018).

Dr. Pignari has been the Technical Program Chair of the ESA Workshop on Aerospace EMC since 2009, and a member of the Technical Program Committee of the Asia Pacific Int. Symp. on EMC since 2010.



Johannes Wolf (Senior Member, IEEE) received the diploma (M.Sc.) and Ph.D. degrees in electrical engineering from the University of Technology, Dresden, Germany, in 1988 and 1994, respectively.

Since March 2022, he is working as a Senior Advisor European Space Technology Center (ESTEC), with the European Space Agency (ESA) in Noordwijk, Netherlands. From 1989 to 1994, he was Assistant Professor at the Institute of Automatic Control at Dresden University of Technology, Dresden, Germany. From 1994 - 1996 he worked as member of

the EMC workgroup in the Institute of Automatic Control at Dresden University of Technology. In 1996 he joined EMC Baden, Baden, Switzerland, where he worked as consulting EMC engineer. 1999 he joined Kayser-Threde GmbH, Munich, Germany, as a System Engineer, working on several projects for the ESA. Since 2001, he has been with the EMC section of the Electrical Department, ESTEC, ESA, Noordwijk, the Netherlands and providing EMC support to projects from Science, Earth observation, Navigation, human spaceflight, and robotic exploration as well as for Launchers. Since 2014, he has been the Head of the EMC section. His research interests include EMC, in particular ESD, powerline communication (on dc lines), experimental procedures, and setups for EMC testing.